## nature electronics

**Article** 

https://doi.org/10.1038/s41928-022-00874-z

# Elastic electronics based on micromeshstructured rubbery semiconductor films

Received: 6 November 2021

Accepted: 17 October 2022

Published online: 28 November 2022

Check for updates

Ying-Shi Guan<sup>1,2</sup>, Faheem Ershad ® <sup>3,4</sup>, Zhoulyu Rao ® <sup>5,6</sup>, Zhifan Ke<sup>7</sup>, Ernesto Curty da Costa<sup>8</sup>, Qian Xiang<sup>9</sup>, Yuntao Lu<sup>5,6</sup>, Xu Wang<sup>2</sup>, Jianguo Mei ® <sup>7</sup>, Peter Vanderslice<sup>8</sup>, Camila Hochman-Mendez<sup>8</sup> & Cunjiang Yu ® <sup>2,3,4,5,6,10</sup> ⊠

The development of soft electronics that can be seamlessly integrated with biological tissue requires intrinsically stretchable rubbery semiconductors with high carrier mobilities. However, the scalable fabrication of rubbery semiconductors remains challenging, particularly using methods that are simple and reproducible. Here we report rubbery semiconductor thin films that are based on a lateral-phase-separation-induced micromesh. A two-polymer blend solution is spin coated on a substrate and forms micromesh morphologies via lateral phase separation, consisting of a continuous organic semiconductor-rich phase and an isolated elastomer-rich phase. The micromesh-structured rubbery semiconductors simultaneously provide efficient charge transport and mechanical stretchability, and by using different polymer blends, we create both p-type and n-type rubbery semiconductor films. The films are used to construct rubbery transistors, complementary inverters and bilayer heterojunction photodetectors that can function even under applied strains of up to 50%. We also create an electronic patch that has a transistor active matrix fully made of rubbery materials and can be used to map the biopotentials of a rat heart.

A mechanically stretchable transistor made out of elastic materials is necessary to build soft integrated electronics<sup>1-3</sup>. To seamlessly integrate and hybridize with soft tissues, the materials must possess mechanical stretchability at the microscopic material level and the macroscopic structural level<sup>4-6</sup>. Among different elastic electronic materials, stretchable semiconductors are particularly important in determining the electrical performances of stretchable transistors and circuits<sup>7-9</sup>. Although efforts have been made to develop elastic semiconductors, the scalable fabrication of elastic rubber-like semiconductors with high carrier mobility and large mechanical stretchability remains a key challenge<sup>10</sup>.

Stretchable semiconductors are typically created via architecture engineering<sup>11-14</sup>, molecular design<sup>7,15</sup> or polymer composite<sup>16-19</sup>. Structures based on architecture engineering, such as in-plane serpentines<sup>13</sup>, wavy structures<sup>11</sup> and kirigami designs<sup>14,20</sup>, can accommodate or eliminate mechanical strain when being stretched due to their structural transformability. However, the semiconductors themselves are intrinsically non-stretchable. Molecular designs—such as the introduction of soft building blocks into a polymer backbone<sup>7</sup> or covalently embedding a semiconducting polymer in a rubber matrix<sup>15</sup>—can provide intrinsically stretchable semiconductors. However, these semiconductors need to have special chemical structures and are only

<sup>1</sup>Institute of Advanced Materials, and School of Chemistry and Chemical Engineering, Southeast University, Nanjing, China. <sup>2</sup>Department of Mechanical Engineering, University of Houston, Houston, TX, USA. <sup>3</sup>Department of Biomedical Engineering, Pennsylvania State University, University Park, PA, USA. <sup>4</sup>Department of Biomedical Engineering, University of Houston, Houston, TX, USA. <sup>5</sup>Department of Engineering Science and Mechanics, Pennsylvania State University, University Park, PA, USA. <sup>6</sup>Materials Science and Engineering Program, University of Houston, Houston, TX, USA. <sup>7</sup>Department of Chemistry, Purdue University, West Lafayette, IN, USA. <sup>8</sup>Regenerative Medicine Research, Texas Heart Institute, Houston, TX, USA. <sup>9</sup>Molecular Cardiology Research Laboratory, Texas Heart Institute, Houston, TX, USA. <sup>10</sup>Department of Materials Science and Engineering, Materials Research Institute, Pennsylvania State University, University Park, PA, USA. ⊠e-mail: cmy5358@psu.edu

applicable to certain organic semiconductors. They, thus, suffer from a lack of generality and complicated organic synthesis. Polymer composites that are prepared by blending the semiconducting polymer with a soft elastomer matrix can provide rubber-like stretchable electronic materials <sup>17,19,21</sup>. However, the approach is still limited to certain microstructures. The stretchable polymer composites that embed semiconducting nanowires or nanofibres into a rubbery matrix are not suitable for general semiconductors <sup>18,22</sup>.

In this Article, we report a stretchable semiconductor film that is based on a lateral-phase-separation-induced micromesh (LPSM). A blended solution of two polymers is spin coated onto a supporting substrate and a sub-micrometre-thick binary-phase microstructureconsisting of a continuous organic semiconductor-rich phase and an isolated elastomer-rich phase—is formed due to the phase separation that occurs during solidification. The structure of the nanocomposite provides efficient charge transport and high mechanical stretchability. We use the approach to create both p- and n-type stretchable semiconductors, with poly(3-hexylthiophene-2,5-diyl) (P3HT) and iso-indigo (P3) used as a p-type semiconducting polymer and poly{ [N,N'-bis(2-octyldodecyl)-naphthalene-1,4,5,8-bis(dicarboximide)-2,6-diyl]-alt-5,5'-(2,2'-bithiophene)} (N2200) used as an n-type semiconducting polymer. These polymers were chosen due to their relatively high charge carrier mobility and manufacturing versatility. Using LPSM semiconductors, we create rubbery transistors, inverters and photodetectors that can retain their electrical functions when being stretched with a strain of up to 50%. To illustrate their potential for soft implantable electronics, we also develop a bioelectronic patch with a rubbery-transistor-based active matrix for multichannel electrocardiogram (ECG) sensing that can be used for the in situ spatiotemporal mapping of the biopotentials of a rat heart.

## LPSM rubbery semiconductor

A schematic of stretchable semiconductor thin-film fabrication based on the LPSM strategy is shown in Fig. 1a. A polymer blend solution drop of the semiconductor and elastomer mixture was applied to a supporting substrate and then spin coated to form a thin film as lateral phase separation took place, and the solvent evaporated to solidify the film. The strong dynamic asymmetry between the semiconductor and elastomer induced by the large difference in molecular size and glass transition temperature between the two components influenced the phase pattern evolution and resulted in viscoelastic phase separation  $^{23,24}$ . Such viscoelastic phase separation drives the formation of unique microsized structures. We started by creating a p-type LPSM rubbery semiconductor, where P3HT was used as the semiconductor precursor and polystyrene-block-poly(ethylene-ran-butylene)-block-polystyrene (SEBS) was used as the elastomer to form the isolated phase (Fig. 1b).

The composite polymer thin films with different weight percentages of P3HT (that is, the weight of P3HT over that of P3HT and SEBS) were prepared, and their morphologies were examined. The detailed preparation of the polymer solution and composite thin films is described in Methods. It is noted that the morphologies of the composite polymer films depend on the weight percentage of P3HT. Figure 1c-h shows a set of optical images of thin composite films with different weight percentages of P3HT. Specifically, films with 75 and 70 wt% P3HT exhibited isolated, circular-shaped SEBS-rich domains that were 0.5-1.0 µm in diameter. Supplementary Fig. 1 shows the atomic force microscopy images of the films. The isolated domain size increased from  $525 \pm 161 \,\text{nm}$  (75 wt% P3HT) to  $820 \pm 232 \,\text{nm}$  (70 wt% P3HT) as the SEBS weight percentage increased from 25% to 30%. An enlarged isolated SEBS-rich domain size was observed for the 65 wt% P3HT thin film and the average diameter was about  $8.83 \pm 3.23 \,\mu m$ (Fig. 1e and Supplementary Fig. 2). As the SEBS weight percentage increased, the isolated domains grew and bridged with one another, generating a new continuous phase (Fig. 1f). Meanwhile, the original continuous P3HT-rich phase shrank to new isolated domains, resulting in phase inversion with further increasing SEBS weight percentage in the composite film (Fig. 1g.h). The morphology formation of the thin composite films and their evolution follow the kinetic and thermodynamic principles<sup>25–28</sup>. The phase morphology evolution shown in Fig. 1c-h follows the viscoelastic phase separation mechanism with a phase inversion phenomenon<sup>24</sup>. In particular, in the 65 wt% P3HT composite film, a microsized mesh morphology was obtained (Fig. 1e). To study the morphology of phase separation, we fabricated the 65 wt% P3HT composite films on different substrates (SiO<sub>2</sub>/Si, glass and polydimethylsiloxane (PDMS)). A similar mesh-like morphology was achieved on different substrates (Supplementary Fig. 3). Generally, the substrates have a negligible effect on the formation of a mesh-like morphology driven by phase separation, which is critical for fully rubbery electronic device fabrication. Further, we studied the film morphology at different annealing temperatures (Supplementary Fig. 4) and different annealing times (Supplementary Fig. 5). The results show that the mesh-like morphology was fairly stable without drastic changes.

Such a binary-phase micromesh morphology with a continuous P3HT-rich phase is advantageous for efficient charge transport (described in more detail later). In addition, the unique mesh structure renders mechanical stretchability, where the continuous P3HT-rich phase provides deformability, whereas the isolated SEBS-rich phase serves as a structure retention module to ensure reversible stretching and releasing. Thereafter, we chose the 65 wt% P3HT composite film (denoted as the LPSM-1 film) to further investigate its microstructures and to employ it for constructing rubbery electronics. The typical thickness of the LPSM-1 film was about 90 nm, based on atomic force microscopy measurement (Supplementary Fig. 6). X-ray diffraction was employed to investigate its molecular packing nature within the LPSM-1 film. As shown in Supplementary Fig. 7a, the X-ray diffraction pattern of the LPSM-1 film exhibits strong (100) and visible (200) diffraction peaks of P3HT at  $5.2^{\circ}$  and  $10.5^{\circ}$ , respectively, which reveals that an ordered structure exists within the LPSM-1 film. Such a packing structure (Supplementary Fig. 7b) is similar to that of the crystalline P3HT nanofibres<sup>29</sup>. Then, to elucidate the micromesh morphology, we studied the top and bottom surface morphology of the LPSM-1 film. As shown in Fig. 1i, j, the two surface topographic structures are almost identical, which suggests lateral phase separation but no vertical phase separation along the thickness direction. To further determine the composition of two phases, we immersed the LPSM-1 film into cyclohexane to selectively wash off SEBS, since SEBS can be dissolved in cyclohexane but P3HT cannot. As shown in the atomic force microscopy image (Supplementary Fig. 8a), after immersion in cyclohexane for about 40 h, the continuous mesh-like phase was maintained, whereas most of the isolated domains were washed off by cyclohexane and only a small portion of residue remained. Thus, the phase separation within LPSM-1 was clear. As depicted in Supplementary Fig. 8b, the continuous mesh-like phase is P3HT rich, and the isolated island domain phase is SEBS rich.

The stretchability of the LPSM-1 film was further investigated. Supplementary Fig. 9a shows that the LPSM-1 film on a thin PDMS substrate can be reversibly stretched and released. The optical images of the LPSM-1 films with 50% strain and without strain are presented in Fig. 1k and Supplementary Fig. 9b, respectively. On cyclic stretching and releasing at a strain of 50%, no visible cracking was observed, indicating that the LPSM-1 film has good mechanical stretchability.

## Rubbery transistor based on LPSM-1 film

The electrical performance of the LPSM-1 film serving as a rubbery semiconductor was evaluated based on rubbery transistors, where all the associated materials have rubber-like stretchability. Specifically, gold nanoparticles (AuNPs) with conformally coated silver nanowires (AgNWs) dispersed within PDMS elastomer (AuNPs-AgNWs/PDMS) served as the conductor, and ion gel served as the dielectric layer<sup>22</sup>. The detailed rubbery electrodes and device fabrication are presented

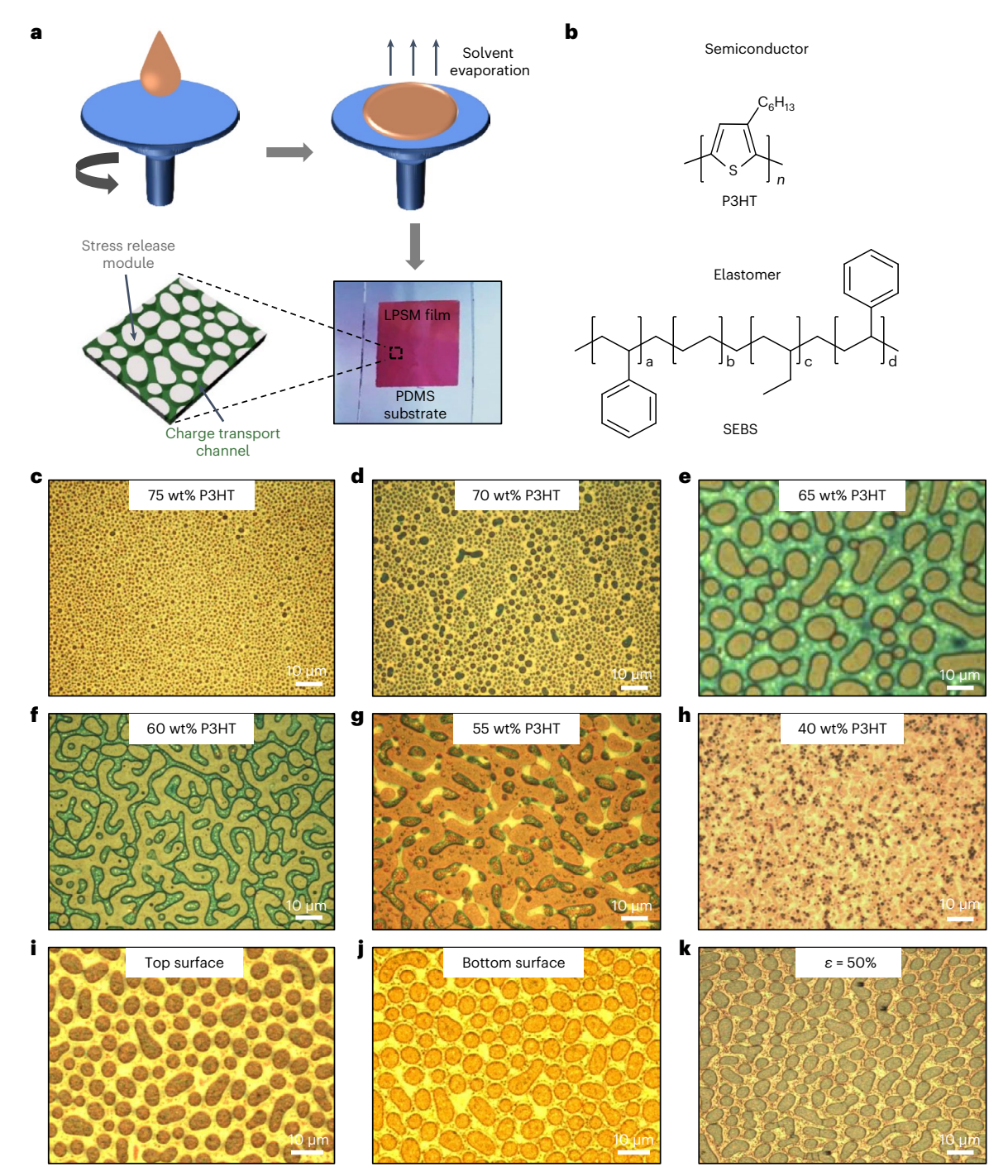
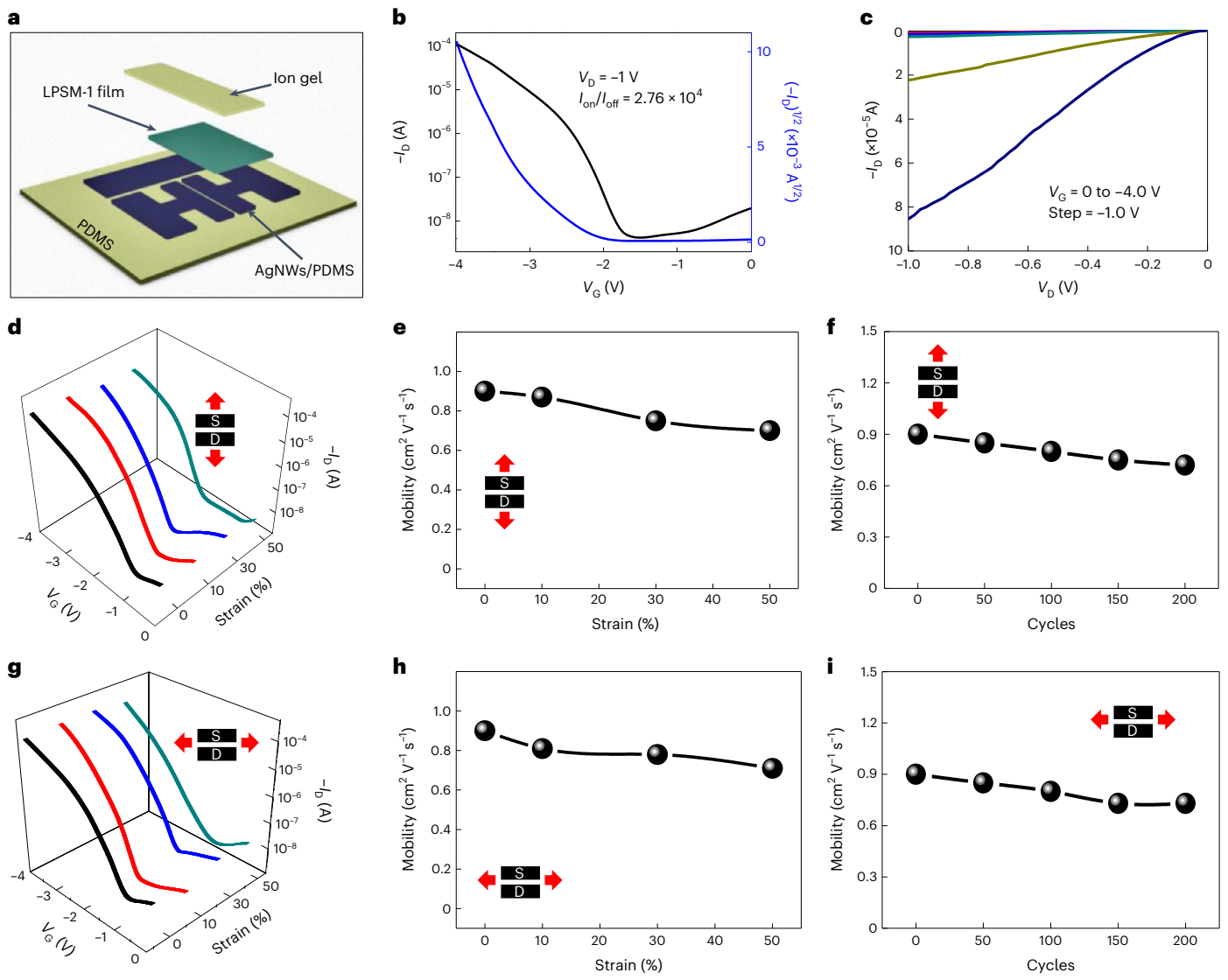


Fig. 1| Fabrication of LPSM rubbery semiconductor. a, Three-dimensional schematic of a rubbery semiconductor with the desired thin-film morphology, which is the core building block of rubbery electronics. b, Chemical structure of P3HT and SEBS.  $\mathbf{c}$ - $\mathbf{h}$ , Optical images of P3HT/SEBS film with different weight

ratios: 75 wt% P3HT ( $\mathbf{c}$ ), 70 wt% P3HT ( $\mathbf{d}$ ), 65 wt% P3HT ( $\mathbf{e}$ ), 60 wt% P3HT ( $\mathbf{f}$ ), 55 wt% P3HT ( $\mathbf{g}$ ), 40 wt% P3HT ( $\mathbf{h}$ ).  $\mathbf{i}$ , 0ptical images of the top surface ( $\mathbf{i}$ ) and bottom surface ( $\mathbf{j}$ ) of the LPSM-1 film in the same location.  $\mathbf{k}$ , 0ptical image of the LPSM-1 film deposited on a PDMS substrate with  $\varepsilon$  = 50% strain.

in Methods. The schematic of the rubbery transistor is shown in Fig. 2a. Figure 2b shows the transfer curve of the rubbery transistor. A typical p-type semiconductor property was demonstrated by a large increase in drain current ( $I_D$ ) when the gate voltage was swept from 0 to -4 V, whereas the drain voltage was fixed at -1 V. The output curve of the transistor is shown in Fig. 2c. The field-effect mobility was calculated to be  $0.90 \,\mathrm{m^2\,V^{-1}\,s^{-1}}$ , and the ON/OFF ratio (that is,  $I_{\mathrm{on}}/I_{\mathrm{off}}$ ) was  $2.76 \times 10^4$ . The carrier mobilities of the semiconducting composite nanofilms with different percentages of P3HT were also investigated (Supplementary Fig. 10).

To examine the transistor performances under mechanical strain, we investigated the electrical properties of rubbery transistors when applying different levels of mechanical strain along and perpendicular to the channel length direction. The transfer curves of the rubbery transistors under 0%, 10%, 30% and 50% uniaxial strain along the channel length direction are shown in Fig. 2d, which clearly show that the rubbery transistors can retain their functions very well even under 50% mechanical strain. The calculated mobilities under different levels of mechanical strain are summarized in Fig. 2e. The mobility value exhibited a slight decrease from 0.90 to 0.75 cm²  $V^{-1}$  s $^{-1}$  when



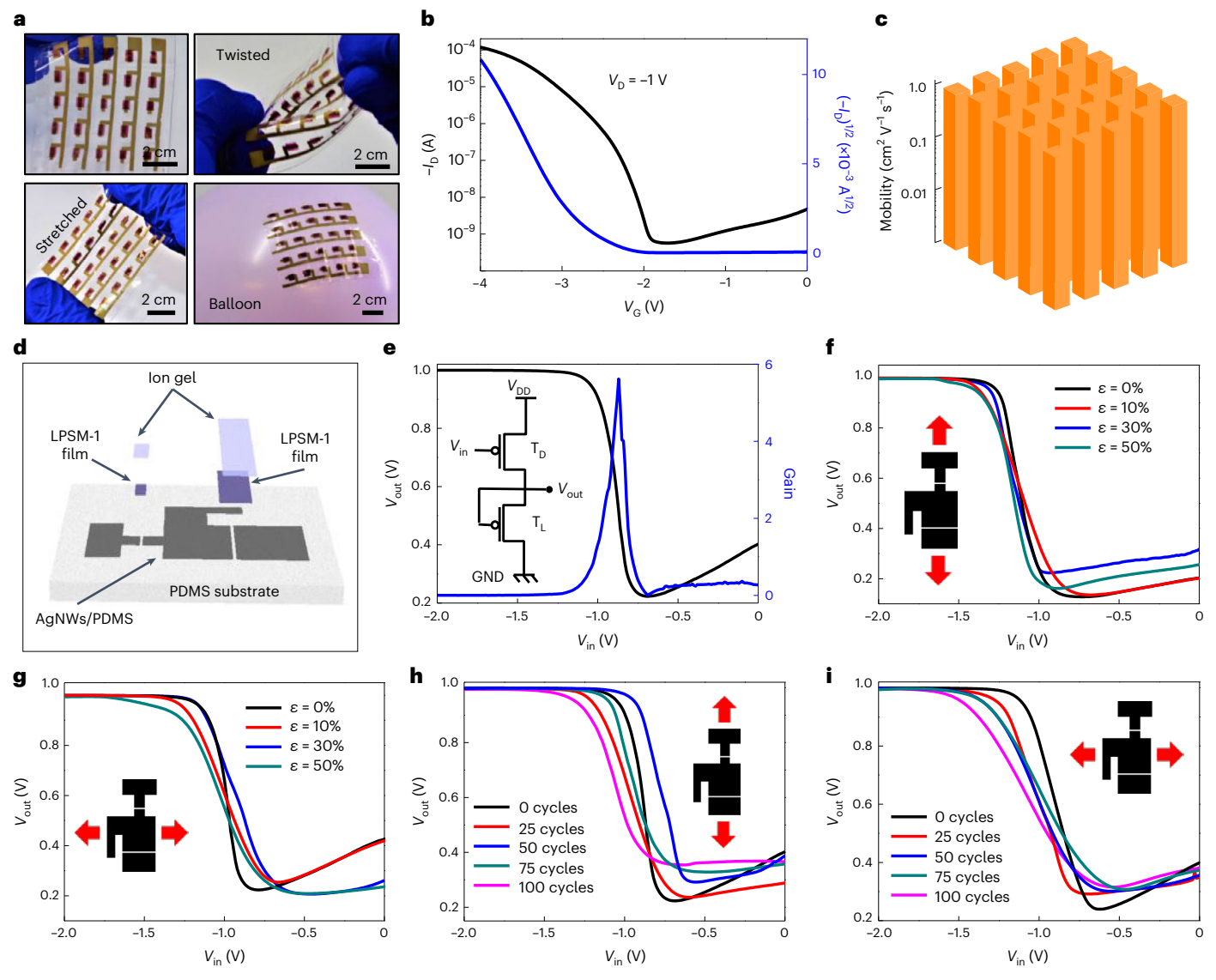
**Fig. 2** | **Rubbery transistor based on LPSM-1 film. a**, Schematic of the rubbery transistor. **b**, Representative transfer curve of the LPSM-1-film-based rubbery transistor. **c**, Representative output curve of the LPSM-1-film-based rubbery transistor. **d**, Representative transfer curves of the rubbery transistor under mechanical strains of 0%, 10%, 30% and 50% along the channel length direction. **e**, Changes in mobility during stretching to 50% strain along the channel length direction. **f**, Changes in mobility after stretch-release cycles

at 30% strain along the channel length direction. **g**, Representative transfer curves of the rubbery transistor under mechanical strains of 0%, 10%, 30% and 50% perpendicular to the channel length direction. **h**, Changes in mobility during stretching to 50% strain perpendicular to the channel length direction. **i**, Changes in mobility after stretch–release cycles at 30% strain perpendicular to the channel length direction.

the device was stretched by 30% strain along the channel length direction, and a moderate decrease to 0.70 cm<sup>2</sup> V<sup>-1</sup> s<sup>-1</sup> when stretched by 50%. The stretch-release cycling test shows that the mobility slightly decreased from 0.90 to 0.72 cm<sup>2</sup> V<sup>-1</sup> s<sup>-1</sup> after 200 cycles of stretching and releasing by 30% strain along the channel length direction (Fig. 2f). Similar results were also observed when the applied strain was perpendicular to the channel length direction (Fig. 2g). The mobility slightly decreases from 0.90 to 0.78 cm<sup>2</sup> V<sup>-1</sup> s<sup>-1</sup> at 30% strain and to 0.71 cm<sup>2</sup> V<sup>-1</sup> s<sup>-1</sup> at 50% strain (Fig. 2h). For comparison, a pure P3HT thin-film-based transistor was fabricated and evaluated under different strains (Supplementary Fig 11). The stretch-release cycling test by stretching and releasing at 30% strain perpendicular to the channel length direction shows that the mobilities initially decrease and then nearly reach a constant value of 0.73 cm<sup>2</sup> V<sup>-1</sup> s<sup>-1</sup> after 200 cycles (Fig. 2i). These results reveal good operating stability of the rubbery transistors based on the LPSM-1 film, high carrier mobility and large mechanical stretchability of the LPSM-1 film.

In addition, a rubbery transistor array was fabricated to demonstrate the device uniformity. The detailed fabrication process is depicted in Supplementary Fig. 12. The transistor array can be stretched, twisted and conformed to a curved surface, demonstrating its good mechanical deformation (Fig. 3a). A representative transfer curve of the transistor array is shown in Fig. 3b. The mobility map of the transistor array exhibited good uniformity (Fig. 3c), with the highest and average mobility value of 1.15 and 0.90 cm $^2$  V $^-$ 1 s $^-$ 1, respectively (Supplementary Fig. 13). The arrayed transistors also showed a uniform ON/OFF ratio (Supplementary Fig. 14). The electrical performances of the LPSM-1-thin-film-based transistor array is summarized in Supplementary Table 1. The hysteresis loop curve of the rubbery transistor is shown in Supplementary Fig. 15, which exhibits a comparable hysteresis for ion-gel-based transistors  $^{9,10}$ .

To demonstrate its potential application in logic circuits, we fabricated LPSM-1-film-based rubbery inverters<sup>30</sup> (Fig. 3d). The detailed fabrication processes of the rubbery inverters are described



 $\label{lem:fig.3} \textbf{Rubbery transistor array and inverter based on LPSM-1 film. a,} \\ \textbf{Fabricated rubbery transistor array under different mechanical deformation modes. b,} \\ \textbf{Representative transfer curve of one transistor from the transistor array. c,} \\ \textbf{Mobility distribution in the rubbery transistor array. d,} \\ \textbf{Schematic of the rubbery inverter. e,} \\ \textbf{Representative VTC of the rubbery inverter. f,g,} \\ \textbf{VTC of} \\ \textbf{OTTATE of the rubbery inverter. f,g,} \\ \textbf{VTC of th$ 

the rubbery inverter under different strains (0%, 10%, 30% and 50%) along ( $\mathbf{f}$ ) and perpendicular ( $\mathbf{g}$ ) to the channel length direction.  $\mathbf{h}$ , $\mathbf{i}$ , Changes in VTCs after stretch–release cycles at 30% strain along ( $\mathbf{h}$ ) and perpendicular ( $\mathbf{i}$ ) to the channel length direction.

in Methods. The rubbery inverter is composed of a p-type driving transistor  $(T_D)$  and a p-type load transistor  $(T_L)$ , with the same channel length and a channel width ratio of 1:4. The representative voltage transfer characteristics (VTCs) of the inverter is shown in Fig. 3e, where the input voltage was swept from -2 to 0 V and the  $V_{DD}$  was fixed at 1 V. We observed that the output voltage of the inverter switched from a high-voltage level to a low-voltage level, displaying correct logic function. The voltage gain of the inverter was calculated to be 5.6. Furthermore, the rubbery inverters can retain their function even with applied mechanical strain along and perpendicular to the transistor channel length direction. The VTCs of the rubbery inverters measured under 0%, 10%, 30% and 50% uniaxial strain along and perpendicular to the channel length direction are plotted (Fig. 3f,g). The inverters can preserve their function. The reversibility and reproducibility of the inverter were further validated by cyclic mechanical stretching at 30% strain. As shown in Fig. 3h,i, the inverters can still correctly function even after 100 cycles with applying 30% strain, showing the mechanical robustness of the LPSM-1-film-based inverters. These

results demonstrate that the rubbery LPSM-1 film can be potentially applied in complex integrated stretchable circuits.

## n- and p-type LPSM semiconductors

To further demonstrate the versatility of this LPSM strategy in creating rubbery semiconductors, we investigated another p-type semiconducting polymer P3 and elastomer polyurethane (PU) (Fig. 4a). Similarly, the weight percentage of P3 had a substantial influence on the morphology of the composite film. The phase morphology evolution is shown in Supplementary Fig. 16. The continuous P3-rich phase shrank to new isolated domains, resulting in phase inversion when the P3 weight percentage decreases from 60 to 50 wt%. This phenomenon indicates that the phase separation of P3 and PU follows the viscoelastic phase separation mechanism as well. After optimizing the P3 weight percentage in the composite film, 60 wt% P3 composite film (denoted as LPSM-2 film) can achieve the micromesh morphology. Then, rubbery transistor devices were fabricated by employing a pure P3 film and an LPSM-2 film as the semiconductor. The same source and

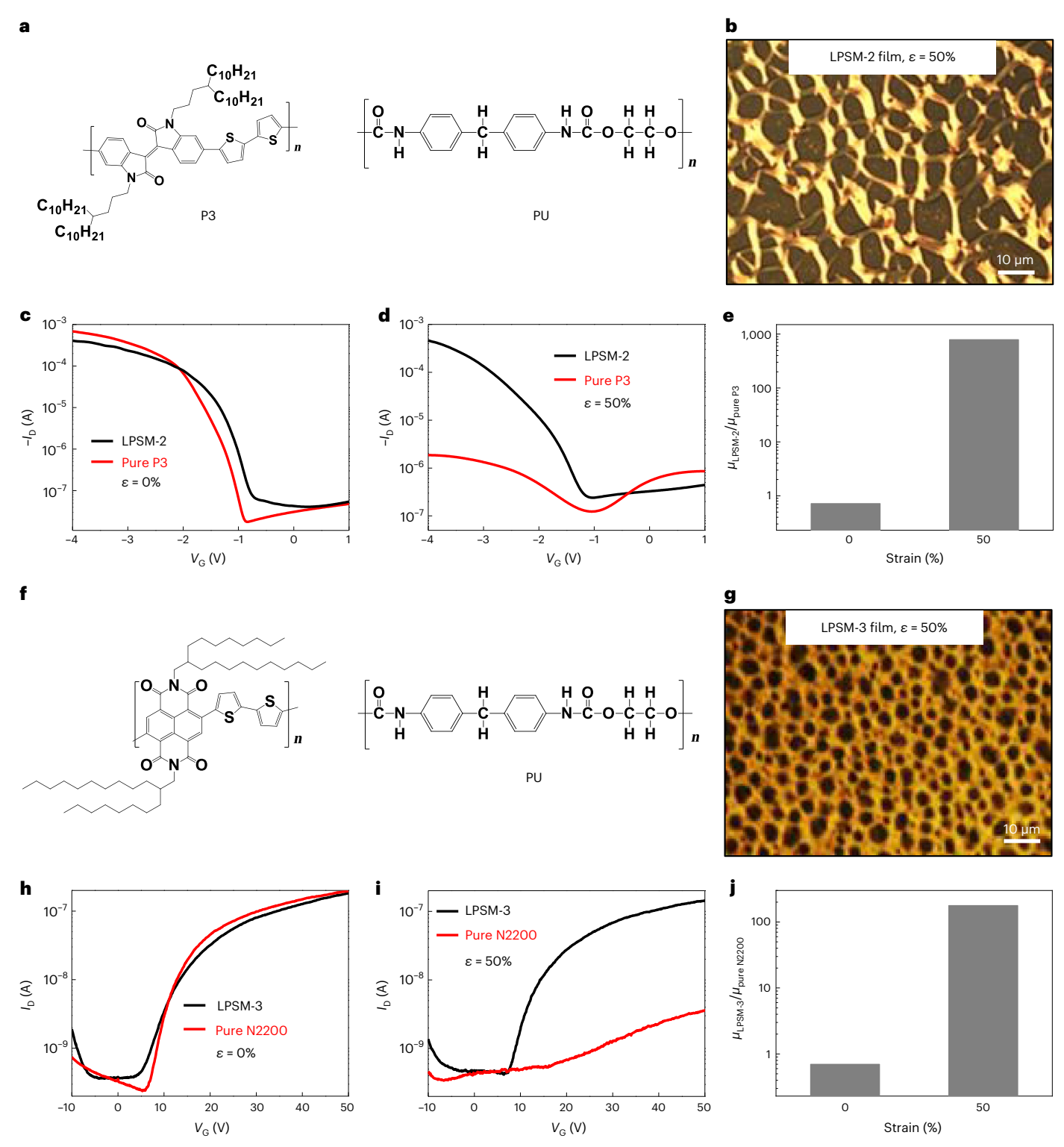


Fig. 4 | n- and p-type LPSM semiconductors. a, Chemical structure of p-type polymer P3 and elastomer PU. b, Optical image of the LPSM-2 film with mesh-like morphology at 50% strain. c, Transfer curve of the LPSM-2 film and pure-P3-film-based rubbery transistor at 0% strain. d, Transfer curve of the LPSM-2 film and pure-P3-film-based rubbery transistor at 50% strain. e, Mobility ratio of the LPSM-2 film and pure P3 film at 0% and 50% strain. f, Chemical structure of the

n-type polymer N2200 and elastomer PU. **g**, Optical image of the LPSM-3 film with mesh-like morphology at 50% strain. **h**, Transfer curve of the LPSM-3 film and pure-N2200-film-based rubbery transistor at 0% strain. **i**, Transfer curve of the LPSM-3 film and pure-N2200-film-based rubbery transistor at 50% strain. **j**, Mobility ratio of the LPSM-3 film and pure N2200 film at 0% and 50% strain.

drain electrodes and ion gel dielectric were used. The detailed device fabrication is described in Methods. The pure P3 film showed severe cracks when subjected to 50% strain (Supplementary Fig. 17), leading to large degradation in mobility. Meanwhile, the LPSM-2 film did not

present any cracks (Fig. 4b) and the mobility showed negligible change when subjected to 50% strain (Fig. 4c-e).

The LPSM strategy was also demonstrated for n-type semiconducting polymer (N2200) and PU elastomer (Fig. 4f). The 50 wt% N2200

composite film (denoted as LPSM-3 film) exhibited the desired micromesh morphology after optimizing the N2200 weight percentage (Supplementary Fig. 18). Rubbery transistors based on the pure N2200 film and LPSM-3 film were constructed using PU as the dielectric layer. The detailed device fabrication is described in Methods. The pure N2200 film exhibited severe cracks whereas the LPSM-3 film showed no cracks when 50% strain was applied (Supplementary Fig. 19 and Fig. 4g). Both ON current and mobility of the pure N2200 film substantially decreased at 50% strain compared with those of the LPSM-3 film (Fig. 4h–j). These results demonstrate the versatility of the LPSM strategy in the making of both n- and p-type rubbery semiconductors.

## Rubbery inverter and photodetector

The complementary-transistor-based inverter (CT inverter) is the fundamental building block of digital circuits and integrated circuits<sup>31,32</sup>. Specifically, in a CT inverter, one p-type and one n-type transistor work in a complementary way (Fig. 5a). We created a rubbery CT inverter composed of a p-type transistor and an n-type transistor by employing the LPSM-2 film and LPSM-3 film as the p-type and n-type semiconductor, respectively. The photograph and schematic of the CT inverter are shown in Fig. 5b and Supplementary Fig. 20, respectively. The detailed fabrication processes of the CT inverter are described in Methods. An input bias  $V_{in}$  (from 0 to 20 V) was applied to the connected gates of the p- and n-type transistors, and the  $V_{\rm DD}$  was fixed at 20 V. The representative VTCs of the inverter are shown in Fig. 5c. The CT inverter showed the correct switching behaviour from a high-voltage level to a low-voltage level. The gain of the CT inverter was calculated to be 5.2. Notably, the rubbery CT inverter operated correctly when different mechanical strains were applied along and perpendicular to the channel length direction. The VTCs of the rubbery CT inverters measured under 0%, 10%, 30% and 50% uniaxial strain along and perpendicular to the channel length direction are plotted in Fig. 5d,e, respectively. The results showed that the rubbery CT inverter retained its functions even under 50% applied mechanical strain. The calculated gain value and switching threshold voltage  $(V_m)$  under different levels of mechanical strain are presented in Fig. 5f. The gain value exhibited a slight decrease from 5.2 to 4.4 when the device was stretched by 30% strain along the channel length direction, and a moderate decrease to 3.2 when stretched by 50%. When the applied strain was perpendicular to the channel length direction, the gain value decreased from 5.2 to 3.3 at 30% strain and then slightly increased to 3.6 at 50% strain. The  $V_{\rm m}$  value showed a slight change when the applied strain was along and perpendicular to the channel length direction (Fig. 5f). Supplementary Table 2 shows the comparison of our fully rubbery CT inverter with reported stretchable inverters.

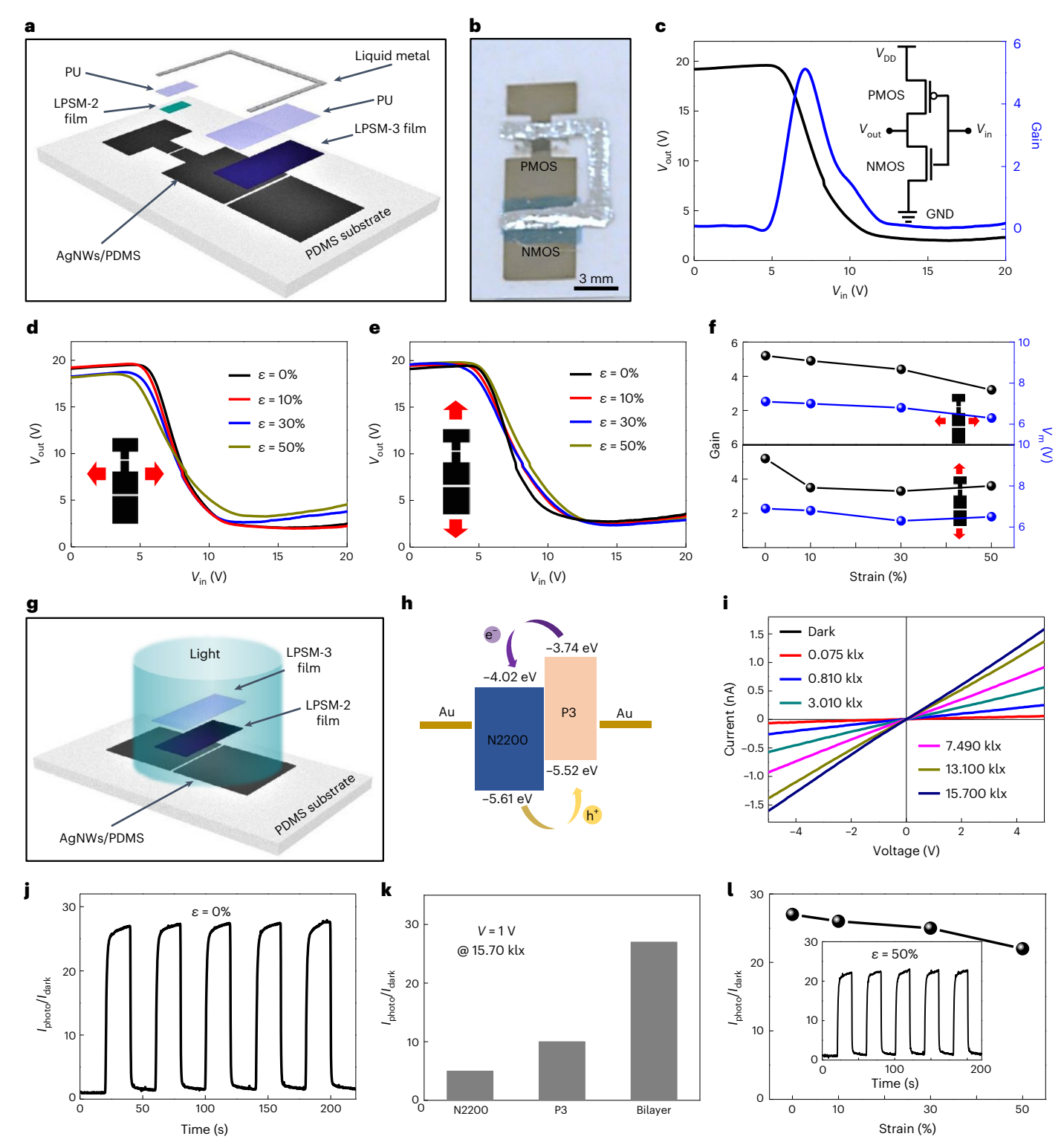
Photodetectors that can convert light inputs into electrical signals have wide applications in light signal detection<sup>33–35</sup>. Stretchable rubbery photodetectors based on the organic bilayer heterojunction structure, using the LPSM-2 film as the donor and LPSM-3 film as the acceptor, were developed. The detailed fabrication processes of the rubbery photodetector are described in Methods. The schematic of the device structure and energy-level diagram of the rubbery photodetector are illustrated in Fig. 5g,h, respectively. Figure 5i shows the current-voltage (I-V) curves of the photodetector in the dark and under white light illumination at different light intensities. At a fixed voltage of 1 V, the time-dependent photocurrent change demonstrated that the device shows a good photoresponse. The current ON/OFF ratio  $(I_{photo}/I_{dark})$  can reach up to 27 (Fig. 5j). The ON/OFF ratio of the bilayer-heterojunction-structure-based photodetector device was much better than that of the devices made from a single layer of the p-type semiconductor (LPSM-2 film) or a single layer of the n-type semiconductor (LPSM-3 film). This is attributed to that fact the donor/ acceptor interface can facilitate photocurrent generation (Fig. 5k and Supplementary Figs. 21 and 22). Figure 51 shows the plot of the ON/OFF ratio of the photodetector versus mechanical strain. The ON/OFF ratio

decreased slightly from 27 at 0% strain to 22 at 50% strain. Supplementary Table 3 shows the comparison of our fully rubbery photodetector with reported stretchable photodetectors. These results suggest that the rubbery photodetectors can work even under 50% strain, demonstrating potential application in various optoelectronics and wearable systems.

## Rubbery active matrix for ECG sensor array

Cardiac action potential monitoring is critical to diagnose pathophysiology of the heart<sup>36-40</sup>. Through the spatial and temporal mapping of the potentials across the curvilinear surface, specific areas of tissue that impede the cardiac potential and result in increased cardiac effort can be revealed<sup>39</sup>. An elastic heart patch based on the rubbery transistor active matrix was constructed to extract the rat heart's electrophysiological metrics, demonstrating its potential application in soft implantable epicardial bioelectronics. To evaluate the capability of the single rubbery transistor to capture ECG signals, it was first used to capture human ECG signals and compared with conventional hospital-grade gel electrodes. Supplementary Fig. 23a shows the schematic of the connection of a human subject, a rubbery transistor and a data acquisition system. As expected, when the rubbery transistor was in the OFF state, no signal could be observed (Supplementary Fig. 23b, top). In the ON state (Supplementary Fig. 23b, middle), the full ECG waveform, including the P, QRS and T waves, is distinct. All the signals were processed with minimal filtering in MATLAB R2018a (Methods), but even after filtering, the ECG signal from the single transistor showed comparatively less noise than that from conventional gel electrodes. The signal-to-noise ratio of the ECG data obtained with the transistor was calculated to be ~40 dB, which shows that the transistor could capture high-quality ECG signals from human skin<sup>41</sup>. Calculation details are reported in Supplementary Note 3 and the power spectrum is shown in Supplementary Fig. 24.

A 4 × 4 rubbery-transistor-array-based active matrix was constructed for the spatiotemporal mapping of the electrical activity from a rat heart. Compared with a previous report on epicardial bioelectronics<sup>6</sup>, the rubbery active matrix here has a slightly higher density of channels distributed over a smaller surface area<sup>42</sup>. The schematic of the rubbery active matrix is illustrated in Fig. 6a and the rubbery active matrix was placed over the right and left ventricles of the in vivo rat heart (Fig. 6b). Details of the surgical procedure are provided in Methods. The rubbery active matrix maintained conformal contact and simultaneously deformed with the beating rat heart. A representative ECG trace of the sinus rhythm (~167 beats per minute (bpm)) from a single sensing node is shown in Fig. 6c. The signal-to-noise ratio was determined to be ~58 dB and this high signal-to-noise ratio is attributed to the increased amplitude of the signal when directly recording signals from the surface of the heart, compared with those recorded from the surface of the skin. The heat maps (Fig. 6c) indicate the propagation of the cardiac action potentials from the upper atria of the heart, to the septum and then to the ventricles of the heart<sup>43</sup>. ECG traces from all the 16 sensing nodes are shown in Supplementary Fig. 25. It should be noted that the heart rate of the rat was lower than usual due to the duration of the experiment, so electrical pacing was conducted to increase the heart rate and mapping was performed again. An electrical stimulator was wired to the heart; the positive electrode was attached to the right ventricle and the negative electrode was attached to the left ventricle (Fig. 6b, inset; blue and yellow stars, respectively). Under pacing, the rat heart rate rose to ~211 bpm (Fig. 6d), and the heat maps coincide with the placement of the stimulation electrodes. As expected, the right ventricle (t = 25 ms heat map; Fig. 6d, bottom left) was activated by the stimulation and propagation proceeded from the right to left side of the heart. Supplementary Videos 1 and 2 show heat maps at 5 ms increments to better illustrate the cardiac action potential propagation over time. These results highlight the potential of fully rubbery implantable bioelectronics for cardiac health monitoring.



 $\label{eq:fig.5} \textbf{Fig. 5} | \textbf{Rubbery CT inverter and photodetector. a}, Schematic of the CT inverter. b, Photograph of the rubbery CT inverter. c, Representative VTC of the rubbery CT inverter under different strains (0%, 10%, 30% and 50%) along (d) and perpendicular (e) to the channel length direction. f, Changes in the gain value and switching threshold voltage of the CT inverter under different strains. g, Schematic of the bilayerheterojunction-structure-based photodetector. h, Energy-level diagram of the bilayer-heterojunction-structure-based photodetector. i, <math>I$ -V curves of

the bilayer-heterojunction-structure-based photodetector under white light illumination with different illuminance values.  $\mathbf{j}$ , Time-dependent photocurrent response of the bilayer-heterojunction-structure-based photodetector at 0% strain.  $\mathbf{k}$ ,  $I_{\text{photo}}/I_{\text{dark}}$  ratio of N2200, P3 and bilayer-heterojunction-structure-based photodetector.  $\mathbf{l}$ ,  $I_{\text{photo}}/I_{\text{dark}}$  ratio of bilayer-heterojunction-structure-based photodetector under different strains. The inset shows the time-dependent photocurrent response of the bilayer-heterojunction-structure-based photodetector at 50% strain.

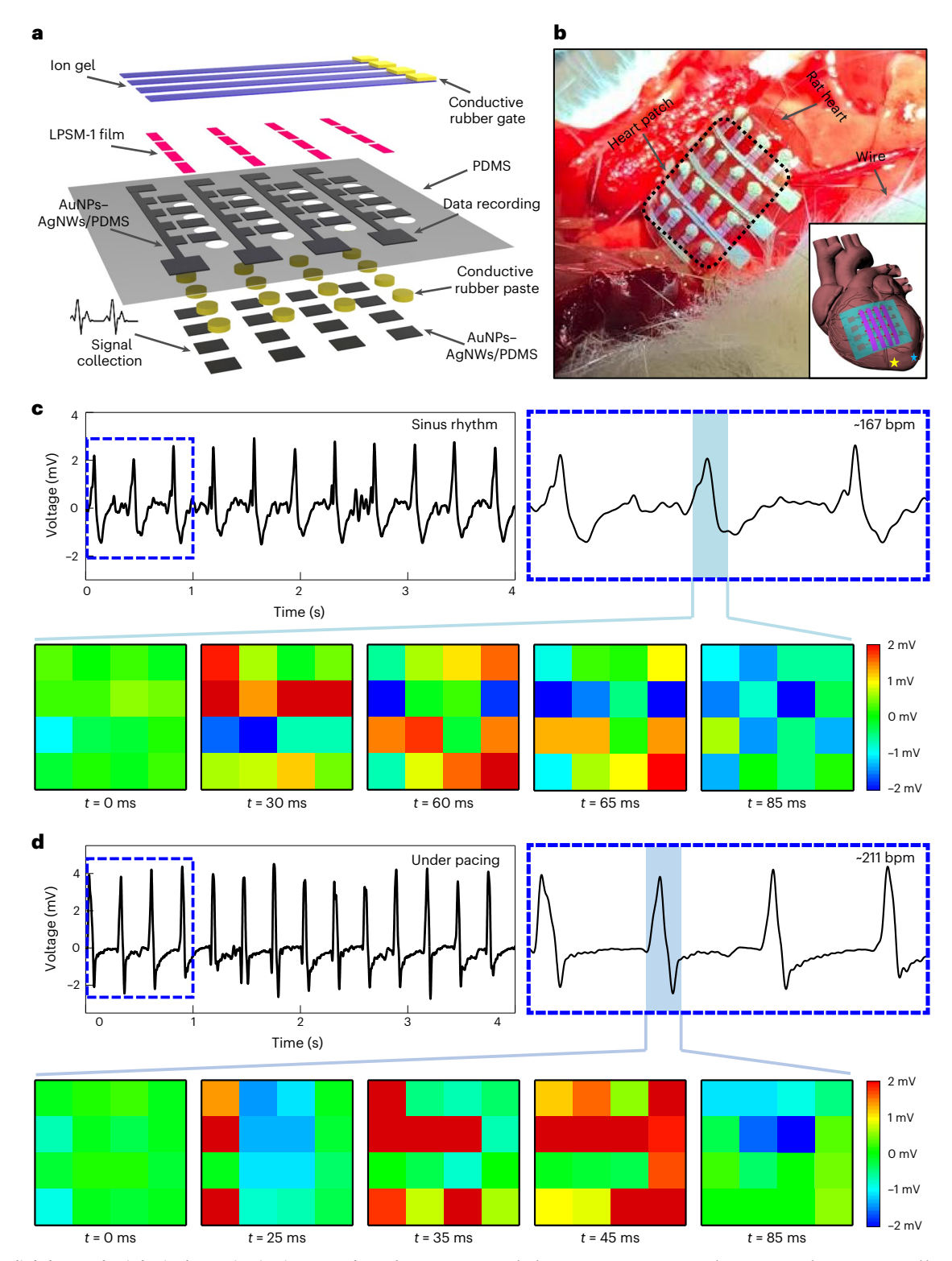


**Fig. 6** | **Epicardial electrophysiological mapping in vivo on rat heart by the fully rubbery transistor active matrix. a**, Schematic of the fully rubbery transistor active matrix. **b**, Photograph of the fully rubbery transistor active matrix on rat heart. The inset shows the spatial position of the active matrix

on the heart.  ${f c}$ , Representative voltage trace and spatiotemporal biopotential mapping results from all the sensing nodes without pacing.  ${f d}$ , Representative voltage trace and spatiotemporal biopotential mapping results from all the sensing nodes under pacing.

## **Conclusions**

We have reported micromesh-structured rubbery semiconductor films that have high mechanical stretchability and relatively high charge mobility. The films were fabricated via the lateral-phase-separation-induced micromesh strategy. Our fabrication

method is simple, uses commercially available materials and does not require additional mechanical structure designs. The resulting films were used to create rubbery transistors, inverters and photodetectors that can maintain their performance at applied strains of 50%. We also fabricated a bioelectronic patch with a rubbery-transistor-based active

matrix for ECG sensing that could be attached to a living rat heart. Rubbery semiconductors based on this simple, scalable and versatile LPSM strategy could be used to develop various soft electronics and integrated circuits for use in applications such as biointegrated electronics<sup>6</sup>, wearable electronics<sup>44</sup> and soft robotics<sup>2,45</sup>.

### **Methods**

#### **Materials**

Anhydrous toluene (>99.0%), SEBS, poly(vinylidene fluoride-co-hexafluoropropylene) (molecular weight, -118,000), poly(vinylidene fluoride-co-hexafluoropropylene) (molecular weight, -400,000), 1-ethyl-3-methylimidazolium trifluoromethanesulfonate (>98.0%), gold chloride trihydrate (>99.9%) and anhydrous ammonia (28.0%) were purchased from Sigma-Aldrich and used as received. Regioregular P3HT was purchased from Sigma-Aldrich, and washed and filtered to remove the low-molecular-weight regioregular P3HT using cyclohexane. N2200 was purchased from Sigma-Aldrich. AgNW (-99.5%) solution (average diameter and length of 120 and 20 mm, respectively) was obtained from ACS Material. PDMS rubber (SYLGARD 184 silicone elastomer kit) was obtained from Dow Corning. The conductive rubber pastes (FL45) were obtained from Zoflex. The surgical adhesive (BioGlue) was obtained from CryoLife.

## Fabrication of the polymer composite film

The elastomer PU was dissolved by tetrahydrofuran ( $25 \, \mathrm{mg \ ml^{-1}}$ ). All the other polymer solutions were obtained by dissolving the polymers in toluene and stirred at  $60 \, ^{\circ}\mathrm{C}$  to dissolve completely. The concentration of the polymer solution is  $5.0 \, \mathrm{mg \ ml^{-1}}$  for P3HT and P3,  $2.5 \, \mathrm{mg \ ml^{-1}}$  for N2200 and  $25.0 \, \mathrm{mg \ ml^{-1}}$  for SEBS. The composite polymer solutions were obtained by mixing the appropriate volume percentages for at least  $1 \, \mathrm{h}$ . The polymer composite films were spin coated ( $1,000 \, \mathrm{rpm}$ ,  $1 \, \mathrm{min}$ ) on different substrates ( $1,000 \, \mathrm{rpm}$ ,  $1 \, \mathrm{min}$ ) on different substrates ( $1,000 \, \mathrm{rpm}$ ), and then activated by exposure to ultraviolet ozone for  $1,000 \, \mathrm{rpm}$ ,  $1 \, \mathrm{min}$ ) or different study.

## Fabrication of the ion gel dielectric layer

To fabricate the ion gel dielectric layer, poly(vinylidene fluoride-cohexafluoropropylene), 1-ethyl-3-methylimidazolium trifluoromethanesulfonate and acetone were blended with a weight ratio 1:4:7 at 70 °C. Then, the solution was cast onto a glass slide and cured for 12 h at 70 °C in a vacuum oven. The obtained ion gel layer can be cut into shapes for use.

## Fabrication of the AuNPs-AgNWs/PDMS electrodes

To fabricate the stretchable AuNPs-AgNWs/PDMS electrodes, first, a shadow mask of Kapton film was manufactured using a programmable cutting machine (Silhouette Cameo). Secondly, the AgNW solution was drop casted onto a cleaned glass slide with the shadow mask followed by curing at  $60\,^{\circ}\text{C}$  for 10 min and then at  $200\,^{\circ}\text{C}$  for 30 min on a hotplate. Third, a premixed PDMS solution (10:1 (w/w) prepolymer/curing agent) was spin coated on the patterned AgNWs at  $300\,\text{rpm}$  for  $60\,\text{s}$ , followed by curing for  $4\,\text{h}$  at  $60\,^{\circ}\text{C}$  to solidify. The PDMS was then peeled off from the glass slide to obtain the patterned AgNWs embedded in PDMS. Fourth, the AgNW/PDMS electrode was immersed in  $0.5\,\text{mM}\,\text{HAuCl}_4\cdot\text{H}_2\text{O}$  aqueous solution for  $2\,\text{min}$  for the Ag-Au galvanic replacement to form AuNPs coated on AgNWs and dipped in NH $_4\text{OH}$  solution (28%) for  $1\,\text{min}$  to dissolve the AgCl layers that were formed on the NWs. Finally, the fabrication of stretchable electrodes was accomplished by washing with deionized water and drying with a  $\text{N}_2\,\text{gun}$ .

## Fabrication of LPSM-1-film-based rubbery transistors

The patterned stretchable AuNPs–AgNWs/PDMS electrodes (source and drain) were prepared as previously reported. Then, the active layers of each device were fabricated by spin coating (1,000 rpm, 1 min) of the 65 wt% P3HT polymer composite solution. After spin coating, thermal

annealing was carried out at  $90\,^{\circ}\text{C}$  for  $60\,\text{min}$  in a vacuum oven. After that, the ion gel layer was laminated onto the polymer thin film as the dielectric layer to complete the device fabrication.

#### Fabrication of LPSM-2-film-based rubbery transistors

The patterned stretchable AuNPs–AgNWs/PDMS electrodes (source and drain) were prepared as previously reported. Then, the active layers of each device were fabricated by spin coating (1,000 rpm, 1 min) of the 60 wt% P3 polymer composite solution. After spin coating, thermal annealing was carried out at 90 °C for 60 min in a vacuum oven. After that, the ion gel layer was laminated onto the polymer thin film as the dielectric layer to complete the device fabrication.

#### Fabrication of LPSM-3-film-based rubbery transistors

The patterned stretchable AuNPs–AgNWs/PDMS electrodes (source and drain) were prepared as previously reported. Then, the active layers of each device were fabricated by spin coating (1,000 rpm, 1 min) of the 50 wt% N2200 polymer composite solution. After spin coating, thermal annealing was carried out at 90 °C for 60 min in a vacuum oven. After that, a PU polymer film was spin coated on top as the dielectric layer to complete the device fabrication.

#### Fabrication of the rubbery inverter

For the fabrication of the rubbery inverters, all the procedures were the same as that of the fabrication of rubbery transistors, except for the AuNPs–AgNWs/PDMS electrodes, which were designed in a different pattern.

#### Fabrication of the rubbery CT inverter

For the fabrication of the rubbery CT inverters, all the procedures were the same as that of the fabrication of rubbery transistors, except that the LPSM-2 film and LPSM-3 film were used as the p-channel and n-channel semiconductor, respectively.

#### Fabrication of the rubbery photodetector

For the fabrication of the rubbery photodetector, the patterned stretchable AuNPs–AgNWs/PDMS electrodes were first prepared. Then, the first active layer of each device was fabricated by spin coating (1,000 rpm, 1 min) of the 60 wt% P3 polymer composite solution. After spin coating, thermal annealing was carried out at 90 °C for 60 min in a vacuum oven. Then, the second active layer of each device was fabricated by spin coating (1,000 rpm, 1 min) of the 50 wt% N2200 polymer composite solution. After spin coating, thermal annealing was carried out at 90 °C for 60 min in a vacuum oven.

## Fabrication of rubbery-active-matrix-based ECG sensor array

The structure of the rubbery-active-matrix-based ECG sensor array is arranged such that the transistor array (top AuNP-AgNW/PDMS; Fig. 6a) and sensing pads (bottom AuNP-AgNW/PDMS; Fig. 6a) are on each side of a single layer of PDMS. The top electrodes were first fabricated using the procedures described for the fabrication of the AuNPs-AgNWs/PDMS electrodes. Then, the bottom electrodes were patterned onto another glass substrate. After spin coating PDMS onto the bottom electrodes, the back side of the top electrodes was carefully aligned and laminated on top of the spin-coated PDMS. The sample was solidified at 60 °C for 4 h, followed by peeling off from the glass slide. Thereafter, via holes were created to interconnect the top electrodes with the bottom electrodes of each sensing node. The conductive rubbery paste (FL45, Zoflex) was used to fill the via holes and was solidified at room temperature for 12 h. The fully solidified conductive rubber paste has substantially strong adhesion to the PDMS substrate without any delamination under a mechanical strain of 50%. At last, the 65 wt% P3HT polymer composite solution was spin coated to form the semiconducting layer. Spin coating through the Kapton-film-based shadow mask allowed for a well-patterned LPSM-1 film, which was annealed at

 $90\,^{\circ}\text{C}$  for  $60\,\text{min}$ . The ion gel pieces serving as the dielectric layer were aligned and laminated on the devices.

#### Electrical characterization

The electrical transport properties were measured under ambient conditions by using a semiconductor analyser (Keithley 4200-SCS) equipped with a probe station (H100, Signatone). Note that we calculated the mobility values on the basis of the specific capacitance of the ion gel (9.8  $\mu F\ cm^{-2}\ at\ 1\ Hz)$  by using an LCR meter (Keysight, U1252B) and an oscilloscope (Agilent, DSO-X-2004A).

#### In vivo animal experiment

All the devices were wired with perfluoroalkoxy-coated stainless steel wires (bare diameter, 76.2 um; coated diameter, 139.7 um; A-M Systems) with conductive rubber paste for the interface to the equipment. After the rat was placed under anaesthesia, the chest was opened to expose the heart. Once the devices were laminated onto the heart, data were collected using the RHD2000 interface board and RHD2132 amplifier (Intan Technologies). A1V d.c. pulse was consecutively applied at 3.5 Hz for electrical pacing using a MyoPacer EP field stimulator (IonOptix). The animal in this study was handled and maintained as per the requirements of the Laboratory Animal Welfare Act (P.L. 89-544) and its 1970 (P.L. 91-579), 1976 (P.L. 94-279) and 1985 (P.L. 99-198) amendments and within the specifications indicated below. Compliance was accomplished by conforming to the standards in the Guide for the Care and Use of Laboratory Animals, ILAR, National Academy Press (revised 2011), and all the procedures were approved by the Texas Heart Institute Institutional Animal Care and Use Committee (#2019-02).

## **Data availability**

The data that support the plots within this paper and other findings of this study are available from the corresponding author upon reasonable request.

#### References

- Chortos, A., Liu, J. & Bao, Z. Pursuing prosthetic electronic skin. Nat. Mater. 15, 937–950 (2016).
- Sim, K., Rao, Z., Ershad, F. & Yu, C. Rubbery electronics fully made of stretchable elastomeric electronic materials. Adv. Mater. 32, 1902417 (2020).
- Zheng, Y.-Q. et al. Monolithic optical microlithography of high-density elastic circuits. Science 373, 88–94 (2021).
- Zhao, X. et al. Soft materials by design: unconventional polymer networks give extreme properties. *Chem. Rev.* 121, 4309–4372 (2021).
- 5. Yuk, H. et al. Dry double-sided tape for adhesion of wet tissues and devices. *Nature* **575**, 169–174 (2019).
- Sim, K. et al. An epicardial bioelectronic patch made from soft rubbery materials and capable of spatiotemporal mapping of electrophysiological activity. Nat. Electron. 3, 775–784 (2020).
- Oh, J. Y. et al. Intrinsically stretchable and healable semiconducting polymer for organic transistors. *Nature* 539, 411–415 (2016).
- 8. Sim, K. et al. Fully rubbery integrated electronics from high effective mobility intrinsically stretchable semiconductors. Sci. Adv. 5, eaav5749 (2019).
- Guan, Y.-S. et al. Air/water interfacial assembled rubbery semiconducting nanofilm for fully rubbery integrated electronics. Sci. Adv. 6, eabb3656 (2020).
- Wang, S. et al. Skin electronics from scalable fabrication of an intrinsically stretchable transistor array. Nature 555, 83–88 (2018).
- 11. Lee, Y. et al. Deformable organic nanowire field-effect transistors. *Adv. Mater.* **30**, 1704401 (2018).
- Lipomi, D. J., Tee, B. C.-K., Vosgueritchian, M. & Bao, Z. Stretchable organic solar cells. Adv. Mater. 23, 1771–1775 (2011).

- 13. Kaltenbrunner, M. et al. Ultrathin and lightweight organic solar cells with high flexibility. *Nat. Commun.* **3**. 770 (2012).
- Zhang, Z. et al. Kirigami-inspired stretchable conjugated electronics. Adv. Electron. Mater. 6, 1900929 (2020).
- Zheng, Y. et al. A molecular design approach towards elastic and multifunctional polymer electronics. *Nat. Commun.* 12, 5701 (2021).
- Choi, D. et al. Elastomer–polymer semiconductor blends for high-performance stretchable charge transport networks. *Chem. Mater.* 28, 1196–1204 (2016).
- 17. Song, E. et al. Stretchable and transparent organic semiconducting thin film with conjugated polymer nanowires embedded in an elastomeric matrix. *Adv. Electron. Mater.* **2**, 1500250 (2016).
- Xu, J. et al. Highly stretchable polymer semiconductor films through the nanoconfinement effect. Science 355, 59–64 (2017).
- 19. Xu, J. et al. Multi-scale ordering in highly stretchable polymer semiconducting films. *Nat. Mater.* **18**, 594–601 (2019).
- Guan, Y.-S., Zhang, Z., Tang, Y., Yin, J. & Ren, S. Kirigami-inspired nanoconfined polymer conducting nanosheets with 2,000% stretchability. Adv. Mater. 30, 1706390 (2018).
- 21. Shin, M. et al. Polythiophene nanofibril bundles surface-embedded in elastomer: a route to a highly stretchable active channel layer. *Adv. Mater.* **27**, 1255–1261 (2015).
- 22. Kim, H.-J., Sim, K., Thukral, A. & Yu, C. Rubbery electronics and sensors from intrinsically stretchable elastomeric composites of semiconductors and conductors. *Sci. Adv.* **3**, e1701114 (2017).
- He, J. et al. Crystallization-arrested viscoelastic phase separation in semiconducting polymer gels. ACS Appl. Polym. Mater. 1, 500–508 (2019).
- Zhu, J., Lu, X., Balieu, R. & Kringos, N. Modelling and numerical simulation of phase separation in polymer modified bitumen by phase-field method. *Mater. Des.* 107, 322–332 (2016).
- Dalnoki-Veress, K., Forrest, J. A., Stevens, J. R. & Dutcher, J. R. Phase separation morphology of spin-coated polymer blend thin films. *Phys. A: Stat. Mech. Appl.* 239, 87–94 (1997).
- Dalnoki-Veress, K., Forrest, J. A. & Dutcher, J. R. Mechanical confinement effects on the phase separation morphology of polymer blend thin films. *Phys. Rev. E* 57, 5811–5817 (1998).
- 27. Karim, A. et al. Phase-separation-induced surface patterns in thin polymer blend films. *Macromolecules* **31**, 857–862 (1998).
- Chung, H.-J., Ohno, K., Fukuda, T. & Composto, R. J. Internal phase separation drives dewetting in polymer blend and nanocomposite films. *Macromolecules* 40, 384–388 (2007).
- 29. Jo, G., Jung, J. & Chang, M. Controlled self-assembly of conjugated polymers via a solvent vapor pre-treatment for use in organic field-effect transistors. *Polymers* 11, 332 (2019).
- 30. Stinner, F. S. et al. Flexible, high-speed CdSe nanocrystal integrated circuits. *Nano Lett.* **15**, 7155–7160 (2015).
- 31. Yoo, H. et al. Reconfigurable complementary logic circuits with ambipolar organic transistors. *Sci. Rep.* **6**, 35585 (2016).
- 32. Lei, T. et al. Low-voltage high-performance flexible digital and analog circuits based on ultrahigh-purity semiconducting carbon nanotubes. *Nat. Commun.* **10**, 2161 (2019).
- 33. Yan, C. et al. An intrinsically stretchable nanowire photodetector with a fully embedded structure. *Adv. Mater.* **26**, 943–950 (2014).
- 34. Li, Q., Guo, Y. & Liu, Y. Exploration of near-infrared organic photodetectors. *Chem. Mater.* **31**, 6359–6379 (2019).
- 35. Yang, D. & Ma, D. Development of organic semiconductor photodetectors: from mechanism to applications. *Adv. Opt. Mater.* **7**, 1800522 (2019).
- 36. Efstratiadis, G., Sarigianni, M. & Gougourelas, I. Hypomagnesemia and cardiovascular system. *Hippokratia* **10**, 147–152 (2006).
- Baid. H., Creed, F. & Hargreaves, J. Oxford Handbook of Critical Care Nursing (Oxford Univ. Press, 2016).

- Mellor, G. J. & Behr, E. R. Cardiac channelopathies: diagnosis and contemporary management. *Heart* 107, 1092–1099 (2021).
- Sánchez-Quintana, D., Doblado-Calatrava, M., Cabrera, J. A., Macías, Y. & Saremi, F. Anatomical basis for the cardiac interventional electrophysiologist. *BioMed Res. Int.* 2015, 547364 (2015).
- Reis, L. A., Chiu, L. L. Y., Feric, N., Fu, L. & Radisic, M. Biomaterials in myocardial tissue engineering. *J. Tissue Eng. Regen. Med.* 10, 11–28 (2016).
- 41. Dixon, A. M. R., Allstot, E. G., Gangopadhyay, D. & Allstot, D. J. Compressed sensing system considerations for ECG and EMG wireless biosensors. *IEEE Trans. Biomed. Circuits Syst.* **6**, 156–166 (2012).
- 42. Gargiulo, S. et al. PET/CT imaging in mouse models of myocardial ischemia. J. Biomed. Biotechnol. **2012**, 541872 (2012).
- 43. Xu, L. et al. 3D multifunctional integumentary membranes for spatiotemporal cardiac measurements and stimulation across the entire epicardium. *Nat. Commun.* **5**, 3329 (2014).
- 44. Sim, K. et al. Metal oxide semiconductor nanomembrane–based soft unnoticeable multifunctional electronics for wearable human-machine interfaces. Sci. Adv. 5, eaav9653 (2019).
- 45. Preston, D. J. et al. A soft ring oscillator. *Sci. Robot.* **4**, eaaw5496 (2019).

## **Acknowledgements**

C.Y. would like to acknowledge the National Science Foundation grants of CAREER (1554499), EFRI (1935291) and CPS (1931893); National Institute Health grant (R21EBO26175); and the Office of Naval Research grant (NOOO14-18-1-2338) under the Young Investigator Program.

## **Author contributions**

Y.-S.G. and C.Y. conceived the concept and designed the work. Y.-S.G., F.E., Z.R., Z.K., E.C.C., Q.X., Y.L. and X.W. performed the experiment.

Y.-S.G., F.E. and E.C.C. analysed the experimental data. Y.-S.G., F.E. and C.Y. wrote the manuscript. All the authors commented and revised the manuscript.

## **Competing interests**

The authors declare no competing interests.

## **Additional information**

**Supplementary information** The online version contains supplementary material available at https://doi.org/10.1038/s41928-022-00874-z.

**Correspondence and requests for materials** should be addressed to Cunjiang Yu.

**Peer review information** *Nature Electronics* thanks Yun-Hi Kim, Longzhen Qiu and Xuanhe Zhao for their contribution to the peer review of this work.

**Reprints and permissions information** is available at www.nature.com/reprints.

**Publisher's note** Springer Nature remains neutral with regard to jurisdictional claims in published maps and institutional affiliations.

Springer Nature or its licensor (e.g. a society or other partner) holds exclusive rights to this article under a publishing agreement with the author(s) or other rightsholder(s); author self-archiving of the accepted manuscript version of this article is solely governed by the terms of such publishing agreement and applicable law.

© The Author(s), under exclusive licence to Springer Nature Limited 2022, corrected publication 2023